IEEE Access
Multidisciplinary ⋮ Rapid Review ⋮ Open Access Journal

Received 2 March 2024, accepted 15 March 2024, date of publication 19 March 2024, date of current version 26 March 2024.

Digital Object Identifier 10.1109/ACCESS.2024.3379235

RESEARCH ARTICLE

A Low-Cost Four-Directional Beamforming Switched Butler Matrix Network Antenna for 5G NR Applications

MING-AN CHUNG, (Senior Member, IEEE), CHIA-WEI LIN, AND CHIH-WEI YANG
Department of Electronic Engineering, National Taipei University of Technology, Taipei 10608, Taiwan

Corresponding author: Ming-An Chung (mingannchung@ntut.edu.tw)

This work was supported by the National Science and Technology Council, Taiwan, under Grant NSTC 112-2221-E-027-065.

ABSTRACT The paper proposes a four-directional beamforming switched antenna system based on Butler matrix for 28 GHz mmWave. It is made up of a 90-degree coupler, a crossover, and a 45-degree phase shifter. A 4 × 4 Butler matrix is combined with a 28 GHz patch antenna to form a Butler network antenna. Four directions of the radiation beam can be changed when the input position is changed. From the simulation and measurement results, the measured reflection coefficients cover 27.9-29.3 GHz at all four ports with a standard reflection coefficient of -10 dB and four different angles of 15°, -46°, +44° and -13° for switching beam direction. The antenna's compact size of 39.1 × 45.6 mm^2 (3.65λ_0×4.26λ_0) makes it ideal for use in millimeter wave bands for 5G NR n258, and n261 applications, while also providing a high gain of 11.5 dBi.

INDEX TERMS Array antenna, Butler matrix, smart antenna, beam switching, millimeter wave.

I. INTRODUCTION

In the past few years, with the rapid increase of wireless communication users, the problems of multipath signal attenuation and mutual interference in the same frequency band have become increasingly important. These problems can be solved by some communication technologies, such as the Multi-Input-Multi-Output (MIMO) antenna [1], [2], [3], [4], [5] or the use of smart antennas to eliminate interference problems. Although MIMO antenna systems have the potential to maximize channel utilization and reduce receiver errors, they are expensive to set up, require high power consumption, and require additional design to increase the isolation between antennas. The beam direction of the smart antenna is controllable, which allows the radiated signal to be directed in a direction with less interference, and indirectly enhances the sensitivity of the receiving antenna. By enabling steering capabilities, the beam array antenna [6], [7], [8], [9], [10] can considerably reduce the cost of the system and reduce the complexity of the overall system. Currently, the 5th generation mobile network (5G) millimeter wave frequency band of the fifth-generation mobile communication, known as 5G FR2, has a frequency of 24.25-52.6 GHz. The 5G millimeter wave (mmWave) communication applications require a beamforming antenna system to overcome the high loss of path in free space [6] and ensure communication quality and stable data transmission.

Currently, beamforming and beam steering is the most effective method to increase the radiation intensity and antenna performance of communication equipment. The study of multibeam array antennas has been extensively explored [7], [11], [12], [13], [14], and there are two methods for implementing antenna beamforming. The first is a phase-steered beamforming array antenna system. For example, the literature [15] has the ability to continuously switch beams in any direction, but requires a more complex circuit structure, including phase shifters, adjustable amplifiers, and switches, which will greatly increase the cost of the system. The second is to use a matrix network to control the direction of the beam in the beamforming antenna system. This method is easier in hardware design, and the production process is simpler. Therefore, when the antenna does not need a precise beam steering function, the passive beamforming matrix structure can be selected. For example: Blass matrix [11],

The associate editor coordinating the review of this manuscript and approving it for publication was Claudio Curcio.

Nolen matrix [16], [17], [18], [19] and Butler matrix [20], [21], [22], [23], [24], [25], [26]. Or use the Ruze lens [27], Rotman lens [28], [29], [30], [31], [32] to change the position of the beam by delaying the beam technology. However, the larger size of the lens is required, which causes problems such as high loss of the beam passing through the lens area. In [33] two types of quadrature couplers are used for good bandwidth in a compact three-by-three Nolen matrix. In [13], a reconfigurable four-polarization switch beamforming technique is utilized in conjunction with a crossed inverted V array antenna. The antenna structure comprises a feed circuit consisting of a double Butler matrix and a V-shaped crossed antenna array. Using planar directors to enhance antenna gain and connecting the dual Butler matrix to two enhanced inverted-V antennas results in the optimal antenna gain. The coupler matrix synthesizes the multibeam array antenna using the generalized joined coupler (GJC) connection coupler matrix, and its structure includes Blass matrix and Nolen matrix [11]. When the phase shifter is adjusted within the matrix, the beam direction of the GJC matrix can be controlled. The twelve antenna array elements fed by the GJC Matrix produce three beam states pointing at $-30°$, $0°$ and $30°$, and increase the transmission efficiency from 95.8% to 97%. In [28], a dual-port phased antenna is presented, featuring two monopoles on each side and a fishbone structure in the middle. The authors propose the Generalized Principle of Pattern Multiplication (GPPM), which employs the antenna to feed two ports and adjust the phase relationship of the signals at the two ports to produce different modes of operation. The Rotman lens multibeam antenna of [29] uses phase gradient transmission lines (PGTL) fed Rotman lens antennas. The antenna structure uses a double layer Rotman lens feed and a patch antenna array at the antenna end to reduce the low loss of the parallel plate. Positioning the feed network in the space separating the antenna array and the Rothman lens leads to a reduced antenna size, while conveying the same idea. The change in output phase variation between the feed ports is used to modify the beam angle direction and to improve the antenna efficiency and gain through the lens at the cost of reduced antenna operating bandwidth. In [30], the design of the reconfigurable antenna utilized the Rotman lens as the beam-forming network. The antenna structure employed six layers of low temperature co-fired ceramics for the substrate, specifically developed for the beam switching array. By setting a phase shift of $30°$ and $90°$ between them, the beam angle can be switched by $-30°$, $-10°$, $10°$ and $30°$. To reduce and make the antenna more compact in size, the antenna is arranged on the top layer of the Rotman lens. By incorporating vector conditioners into beam switching networks, it is possible to mitigate the high insertion loss of RF switches. Furthermore, a vector adjuster can facilitate beam direction switching. In [31], the Trifocal Rotman Lens Beamforming Network (TFRL-BFN) is used. A metal cavity is formed within the Rotman lens by enclosing the TFRL-BFN with a pair of metal parallel plates. The Rotman lens then functions as a beamformer. The structure has seven feed ports and eight antenna ports, with three focal beams separated by thirty degrees at the output. In the millimeter wave phase controlled antenna of [32], vertically installed planar transition (VIPT) and flexible plates are used in combination, eliminating the need for expensive RF connectors and reducing matching adjustments. Furthermore, the VIPT vertical plate is interchangeable, enabling it to be swapped out for various designs and requirements. The beam angle can reach 32 different directions, and the overall angular coverage is $70°$, with extremely low reflection and low insertion loss. Integrates two Rotman lenses for the beam switching function. Finally, a VIPT flexible substrate can increase the overall heat dissipation area.

Blass, Nolen, and Butler matrices use couplers and phase shifters to create beamforming networks. Unlike lens beamforming technologies, all offer the advantages of compact size and low path loss. Among the three, the Butler matrix stands out with its simple structure, large bandwidth, and cost-effectiveness, requiring fewer couplers and phase shifters than the other two for the same compact size. However, it has limitations on the number of ports, requires cross-coupler or multilayer network designs, and may have higher side lobe levels, as mentioned in the literature [30]. Numerous papers on Blass matrix design [20], [21], [22], [23], [24], [25], [26], [34] employ single, double, and multilayer substrates, incorporating metamaterial transmission line (MTM-TL), branch line coupling (BLC) and substrate integrated waveguide (SIW) structures. It is possible to design it in three matrix configurations: 4×4, 8×8, and 16×16 matrices. By adjusting the input port feeding, the direction of the antenna beam can be controlled by manipulating the phase of the signal at the output of the matrix network. In recent years, the Butler matrix antenna substrate has been derived from various structures, such as the parallel plate waveguide (PPWG) [19], [33], [34], [35], a new dual layer dielectric substrate in which a slotted line is sandwiched between two dielectric backing layers, and Butler Matrix beamforming circuits for millimeter band applications.

In [21], a wideband, high-gain, all-metal multilayer parallel plate slot array antenna was used to mitigate unwanted resonances that may occur within the metal between the slotted plates. In [36] uses an all-metal multilayer parallel plate structure to design a gap array antenna with high gain characteristics. The components required in the Bart matrix are fabricated using structures such as the printed ridge gap waveguide (PRGW) [20], [37], [38], [39], SIW [24], [25] and microstrip [15], [20]. Although utilizing a multilayer substrate can reduce the issue of stray radiation, it typically comes with a higher production cost compared to single-layer boards.

The antenna is designed with a single-layer substrate and is constructed using a 4×4 Butler matrix network for beam switching. The combination of coupler, phase shifter, and cross-coupler components is used. Four 28GHz patch antennas are used at the antenna end. The substrate is Rogers RT/duroid 5880 with a thickness of 0.254 mm, and the

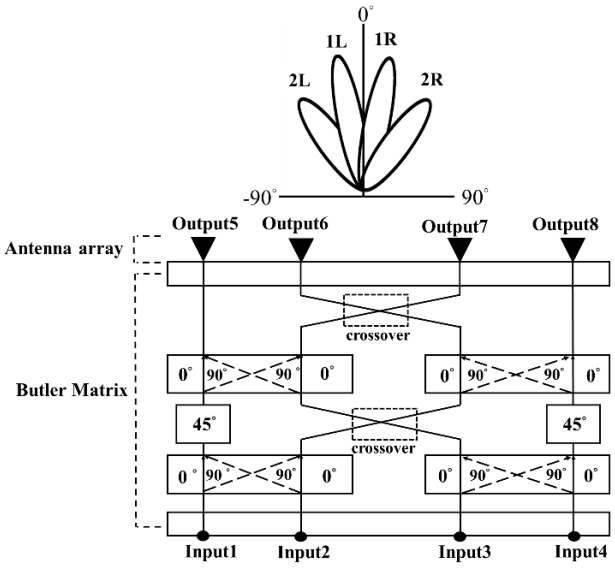

FIGURE 1. 4 × 4 Butler matrix antenna architecture.

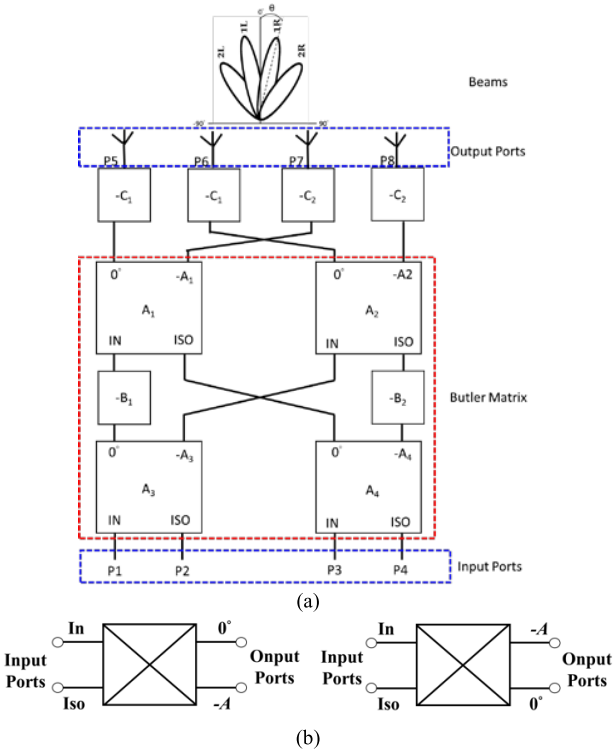

FIGURE 2. (a) 4 × 4 Butler matrix network. (b) Input and output network of the converter.

dielectric constant is 2.2. The structure size of the Butler matrix antenna is 39.1 × 45.6 mm^2 ($3.65\lambda_0 \times 4.26\lambda_0$).

II. BUTLER MATRIX DESIGN

A. BUTLER MATRIX ANTENNA

The Butler matrix architecture consists of four parts: a hybrid coupler, a phase shifter, a crossover, and an array antenna. Fig. 1 shows the schematic diagram of the 4 × 4

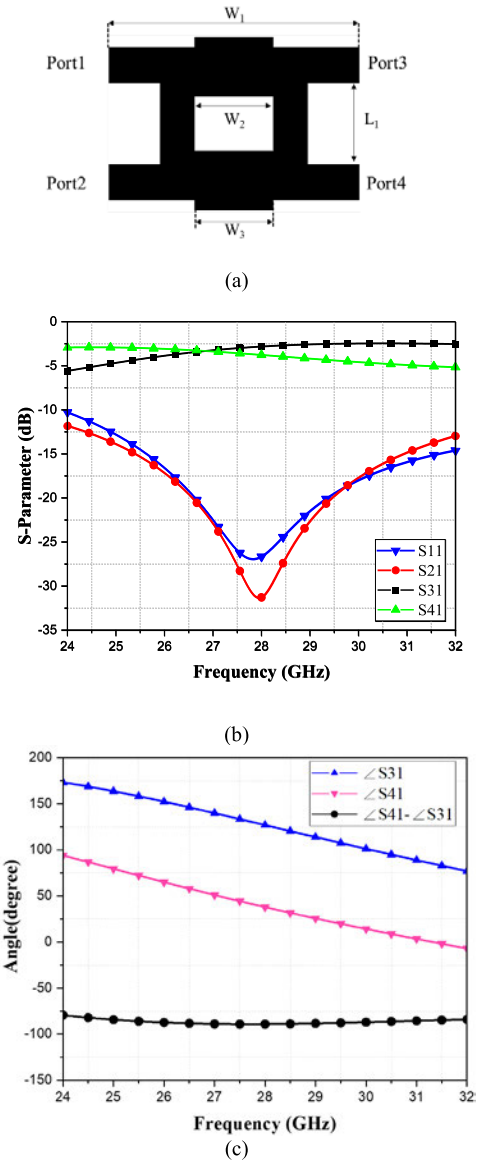

FIGURE 3. (a) 90-degree coupler structure. (b) Simulation of the S-parameter of the 90-degree coupler at 28Ghz Port1. (c) Phase simulation of 90-degree coupler feeding in 28Ghz Port1. The parameters in units (mm) are as follows: W_1 =5.25mm. W_2 =1.65mm. W_3 =1.65mm. L_1 =1.7mm.

Butler matrix. When four different input ports are used, phase differences of -45, 135, -135, and 45 degrees are generated at the output after excitation. And change the radiation beam angle to 15 degrees (1R), -45 degrees (2L), 45 degrees (2R), -15 degrees (1L). Fig. 2(a) has inputs P1-P4 and output P5-P8, and is composed of four (A1-A4) 90-degree couplers. The phase difference of the 90-degree coupler output port is -A1 or -A2, consisting of Fig. 2(b). When P1 to P4 are inputs individually, the corresponding phases generated by the Butler matrix are shown in Table 1. When feeding from each of the four input ports, a fixed phase can be changed to achieve the beam switching effect. Table 2 shows the ideal corresponding phase table for the input ports and output ports.

TABLE 1. Butler matrix corresponds to the phase.

	Port 5	Port 6	Port 7	Port 8
Port 1	$-B_1-C_1$	$-A_3-C_1$	$-B_1-A_1-C_2$	$-A_2-A_3-C_2$
Port 2	$-B_1-A_3-C_1$	$-C_1$	$-B_1-A_1-A_3-C_2$	$-A_2-C_2$
Port 3	$-A_1-C_1$	$-B_2-A_2-A_4-C_1$	$-C_2$	$-B_2-A_4-C_2$
Port 4	A_1+A_4+C1	$-B_2-A_2-C_1$	$-A_4-C_2$	$-B_2-C_2$

TABLE 2. 4 × 4 Butler matrix corresponding phase.

	Output 5	Output 6	Output 7	Output 8	Output phase difference	Beam angle (θ)
Input 1	-45°	-90°	-135°	-180°	-45°	15° (1R)
Input 2	-135°	0°	-225° (135°)	-90°	135°	-45° (2L)
Input 3	-90°	-225° (135°)	0°	-135°	-135°	45° (2R)
Input 4	-180°	-135°	-90°	-45°	45°	-15° (1L)

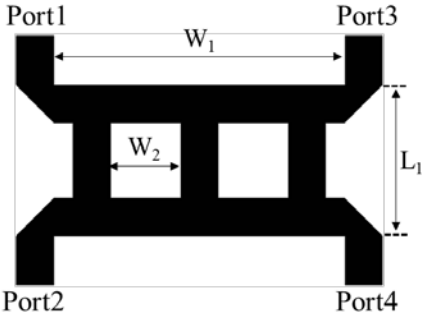

(a)

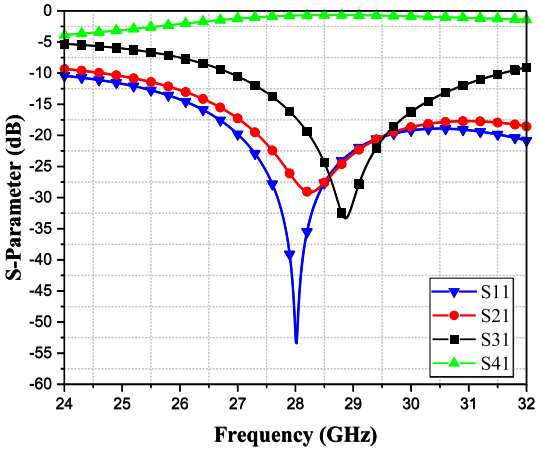

(b)

FIGURE 4. (a) Crossover structure. W_1 =5.58mm. W_2 =1.6mm. L_1 =3.02mm.

B. 90 DEGREE COUPLER

1) 90 DEGREE COUPLER DESIGN

Fig. 3(a) shows the simulated structure of a 90-degree coupler with a chosen frequency of 28 GHz. The input is Port1,

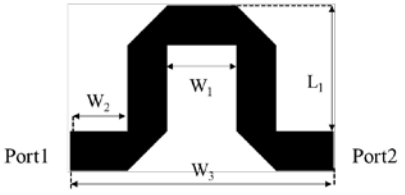

(a)

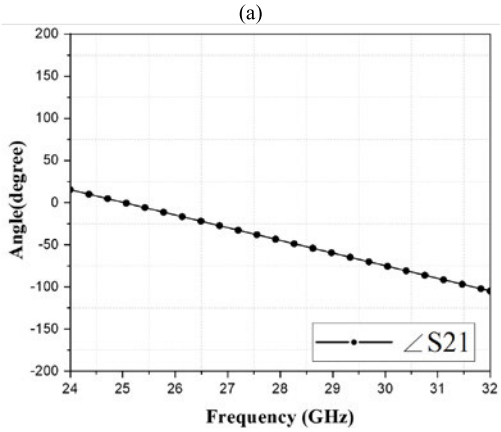

(b)

FIGURE 5. (a) 45-degree phase shifter structure. (b) 45-degree phase. The parameters in unit(mm) are: W_1 =1.32mm. W2=1.1mm. W_3 =5.02mm. L_1 =2.39mm.

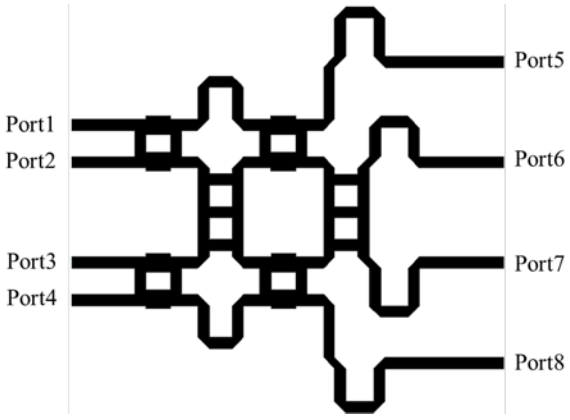

FIGURE 6. 4 × 4 Butler matrix structure.

the isolation is Port2, and the outputs are Port3 and Port4. Fig. 3(b) shows the 90-degree coupler at 28 GHz.

The S11 and S21 are both less than the -10 dB standard at 24-32 GHz, and at 28 GHz S31 is -2.8 dB and S41 is -3.7 dB. The simulated phase difference between S31 and S41 at28 GHz is -89 degrees when the input is Port1, as shown in Fig. 3(c).

C. CROSS COUPLER DESIGN

Simulate a cross coupler with a frequency of 28 GHz, and simulate four ports. The architecture of the cross coupler is shown in Fig. 4(a). The frequency point is 28 GHz and is input by Port1. The measured results show that both the reflection coefficient (S11) and the isolation coefficient (S21 & S31)

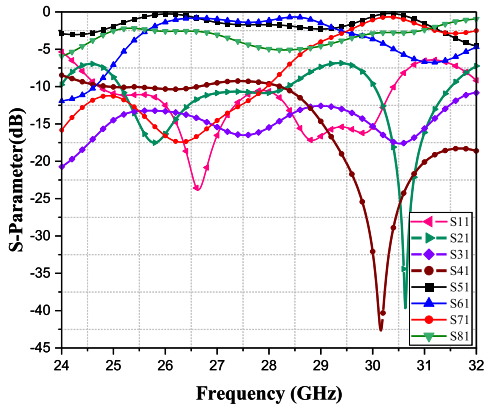

(a)

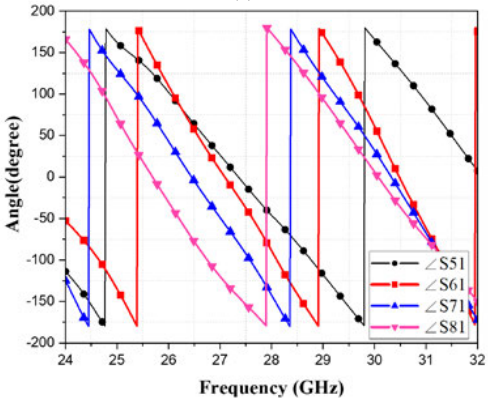

(b)

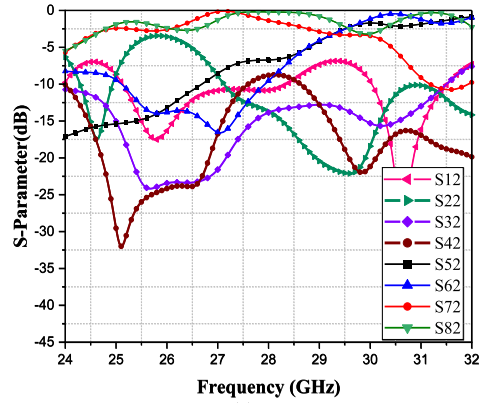

(c)

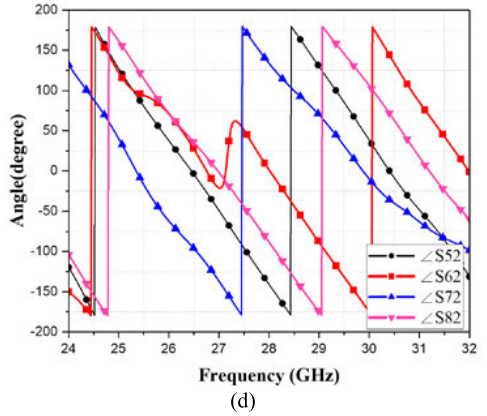

(d)

FIGURE 7. (a) Port1 feeds into the S-parameter simulation. (b)Port1 feeds the corresponding phase difference. (c)Port2 feeds into the S-parameter simulation. (d)Port2 feeds the corresponding phase difference.

are below −25dB, while the insertion loss (S41) is 0.73 dB. Fig. 4(b) illustrates the S-parameter results.

D. 45-DEGREE PHASE SHIFTER DESIGN

Use high-frequency electromagnetic simulation software to simulate a 45-degree phase shifter. Fig. 5(a) realizes the phase gap between Port1 and Port2 by changing the microstrip. Fig. 5(b) shows that the phase shifter produces a -45-degree phase difference at 28 GHz. relationship, the S-parameter and phase simulation of the output port 5-8 is only carried out for the feed-in Port1 and Port2.

E. 4 × 4 BUTLER MATRIX

Fig. 6 shows a 4 × 4 Butler network combining 90 hybrid coupler, crossover, and 45-degree phase shifter. It is a symmetrical structure. Port1 and Port4 are symmetrical, and their ideal output phase difference is ±45 degrees. Port2 and Port3 are also symmetrical, and their ideal output phase difference is ±135 degrees. Due to the symmetrical relationship, the S-parameter and phase simulation of the output port 5-8 is only carried out for thefeed-inPort1andPort2.

When the input is port 1, the reflection coefficient change is observed from the output ports 5 to 8, as shown in Fig. 7(a). At the analog frequency point of 28 GHz, the S11 value is below −10 dB, indicating good impedance matching. The isolation performance between Port 1 and Ports 2, 3, and 4 is satisfactory, with S21 at −12 dB, S31 at −15 dB, and S41 at −10 dB. Additionally, when the frequency is 28 GHz, the transmission capability is demonstrated by S51 at −1 dB, S61 at −2 dB, S71 at −7 dB, and S81 at −5 dB, with an average value of −5 dB. The average value is −5 dB, indicating good transmission capacity. Fig. 7(b) shows that

when the frequency point is 28 GHz, the phase shift between Port5 to Port8 will be caused by feeding in the input Port1, which are S15 (−46 degrees), S16 (−88 degrees), S17 (−135 degrees), and S18 (−187 degrees). When Port1 corresponds to Port5 to Port8, the ideal phase gap between the two adjacent the output port is −45 degrees. From the simulation results, the phase variation between the adjacent outputs is −45±7 degrees, and it is still within the acceptable range compared to the ideal phase difference.

Following the procedure mentioned above, the excitation is subsequently applied through Port 2, allowing the observation of S-parameter variations between Port 5 and Port 8. As illustrated in Fig.7(c), clear evidence emerges, demonstrating that at the analog frequency of 28 GHz, the S22 parameter manifests a value below −10 dB, indicating excellent impedance matching. In particular, the isolation performance between input Port 1 and Ports 2, 3, and 4 is effectively evaluated, revealing S12 at −12 dB, S32 at −13 dB, and S42 at −10 dB. Furthermore, when the frequency point corresponds to 28 GHz, the corresponding S-parameter values exhibit S52 at −7 dB, S62 at −7.5 dB, S72 at -2 dB, and S82 at 0 dB. The average loss value is −7 dB, indicating good conduction capability. Fig.7(d) shows that when the analog frequency point is 28 GHz, the phase gap between

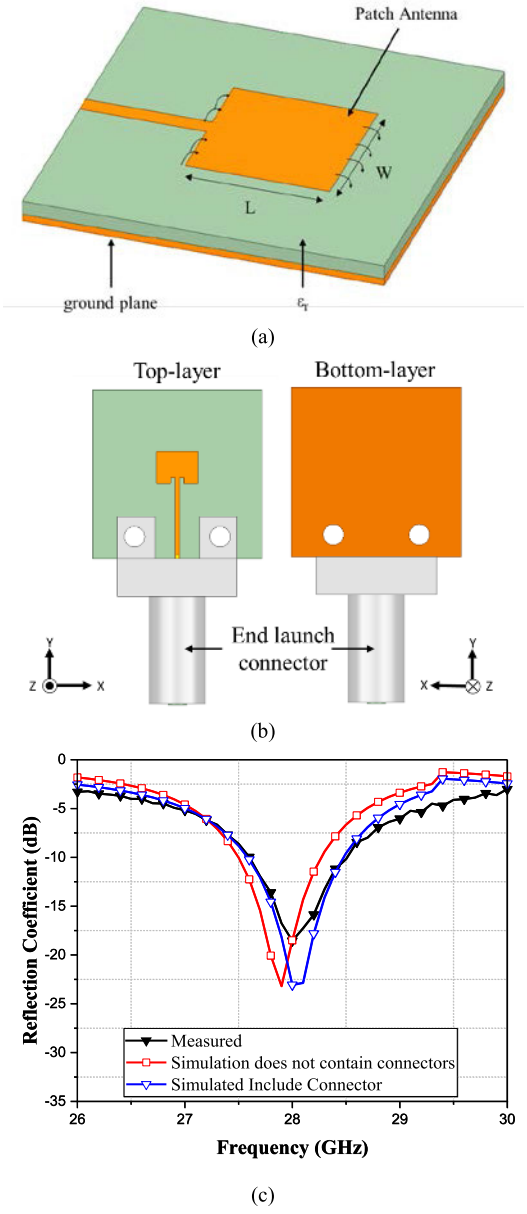

FIGURE 8. (a) Patch antenna. (b) 28 GHz patch antenna includes end launch. (c) Reflection coefficient.

Port5 to Port8 will be caused by feeding in the input Port2. They are the symbols of angles ∠S52 (−135 degrees), S62 (0 degrees), S72 (135 degrees), and S82 (−90 degrees). When the input Port2 corresponds to Port5 to Port8, the ideal phase gap between the two adjacent output ports is −135 degrees. Based on the simulation data presented, the adjacent phase difference of each output terminal is found to be within an acceptable range compared to the ideal phase difference, with a deviation of only −135±4 degrees.

Table 3 compares the ideal phase with the four input ports. When Port1-Port4 are input, the phase angles of Port5 to Port8 in the simulated and ideal comparisons differ by seven degrees, two degrees, two degrees, and five degrees, respectively. Since the 4 × 4 Butler matrix simulated plate has a non-ideal loss coefficient, the simulated phase is still different from the ideal phase.

TABLE 3. 4 × 4 Butler matrix ideal phase and analog phase comparison.

	Port5	Port6	Port7	Port8	Phase
Port1 (Ideal)	-45°	-90°	-135°	-180°	-45°
Port1 (Simulated)	-46°	-88°	-135°	-173°	-45°±7
Port2 (Ideal)	-135°	0°	-225° (135°)	-90°	135°
Port2 (Simulated)	-140°	1°	133°	-88°	135°±2
Port3 (Ideal)	-90°	-225° (135°)	0°	-135°	-135°
Port3 (Simulated)	-92°	131°	0°	-134°	-135°±2
Port4 (Ideal)	-180°	-135°	-90°	-45°	45°
Port4 (Simulated)	-178°	-131°	-91°	-43°	45°±5

F. 28 GHZ PATCH ANTENNA ELEMENT

It is connected to 28 GHz patch antennas for signal excitation at the four output ports. The patch antenna is shown in Fig. 8(a), while the design can be calculated using(1)-(4) [35].

$$f_c = \frac{V_C}{2L_{eff}\sqrt{\varepsilon_{eff}}} = \frac{1}{2\,(L+2\Delta L)\sqrt{\varepsilon_{eff}}\sqrt{\mu_0\varepsilon_0}} = q\frac{V_C}{2L\sqrt{\varepsilon_0}} \tag{1}$$

$$\varepsilon_{eff} = \frac{\varepsilon_r+1}{2} + \frac{\varepsilon_r-1}{2}\frac{1}{\sqrt{1+\frac{12W}{h}}} \tag{2}$$

$$W = \frac{1}{2f_{rc}\sqrt{\varepsilon_{eff}}\sqrt{\mu_0\varepsilon_0}}\sqrt{\frac{2}{\varepsilon_r+1}} = \frac{V_c}{2f_r}\sqrt{\frac{2}{\varepsilon_r+1}} \tag{3}$$

$$L = \frac{1}{2f_{rc}\sqrt{\varepsilon_{eff}}\sqrt{\mu_0\varepsilon_0}} - 2\Delta L \tag{4}$$

The speed of light is *Vc*. Permittivity of the free space is, and the magnetic permeability is the length is L, width is W, thickness is h, the effective length of the microstrip is, Fringe Factor is *q*, and the relative permittivity and equivalent permittivity are and respectively.

To generate a switchable radiation beam, a Butler matrix needs to be connected

to an array patch antenna. In accordance with the microstrip antenna theory, an array antenna operating at 28 GHz is designed using a patch antenna, illustrated in Fig. 8(b). Then use the high-frequency electromagnetic simulation software to design the 28 GHz patch antenna and add the end launch fixture to simulate the reflection coefficient. As depicted in Fig. 8(c), the reflection coefficients exhibit a striking resemblance between the scenarios where the end launch fixture is present and absent. Subsequent adjustment and optimization for the patch antenna can eliminate the influence of the end launch.

Simulation Analysis of 4 × 4 Butler Matrix Beam Switching Design Fig. 9 is the dimensions of 4 × 4 Butler matrix, and the dimensions are in Table 4. Screw holes are incorporated into the substrate's edge to ensure compatibility with the End launch connector, which feeds the signal and prevents

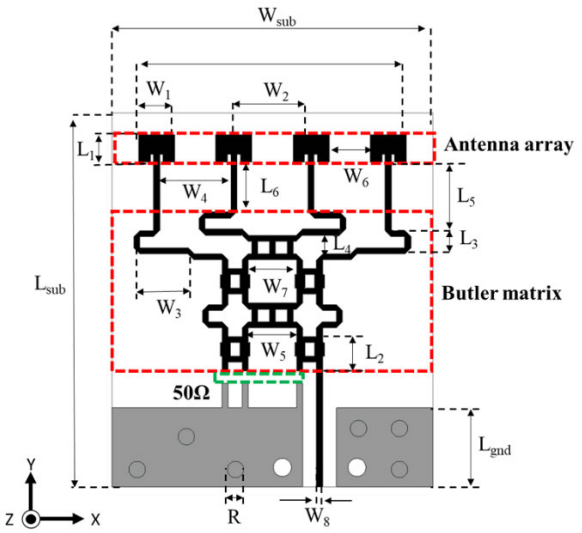

FIGURE 9. 4 × 4 Butler matrix dimensions.

TABLE 4. 4 × 4 Butler matrix antenna dimensions (Unit: mm).

Parameter	L_1	L_2	L_3	L_4	L_5
Value	3.37	5.25	2.82	2.27	8.34
Parameter	L_6	W_1	W_2	W_3	W_4
Value	6.06	4.42	9.42	5.58	1.13
Parameter	W_5	W_6	W_7	W_8	W_{sub}
Value	5.86	5	5.86	0.254	39.15
Parameter	L_{sub}	L_{gnd}	R		
Value	45.64	9.63	2		

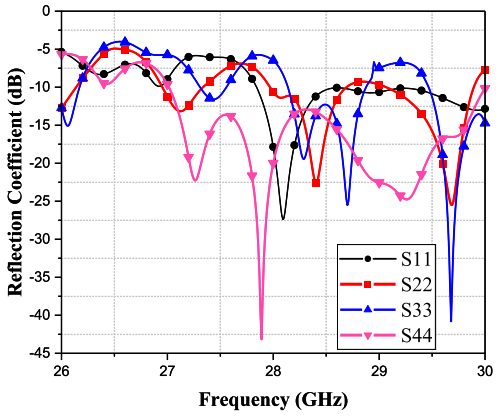

FIGURE 10. Reflection coefficient simulation.

interference with the antenna radiation while meeting the required specifications. In Fig. 10 the simulation results of reflection coefficients of Port1 to Port4 (S_{11}, S_{22}, S_{33}, S_{44}).

Under the standard of reflection coefficient below −10 dB. It can be observed that Port1 (S_{11}) is 27.8-30 GHz. Port2 (S_{22}) is 27.9-28.6 GHz and 29-29.8 GHz, Port3 (S_{33}) is 27.8-28.8 GHz, and Port4 (S_{44}) is 27-30 GHz. The simulation results indicate that the reflection coefficients of Port1 to Port4 are at 28.2-29.8GHz.

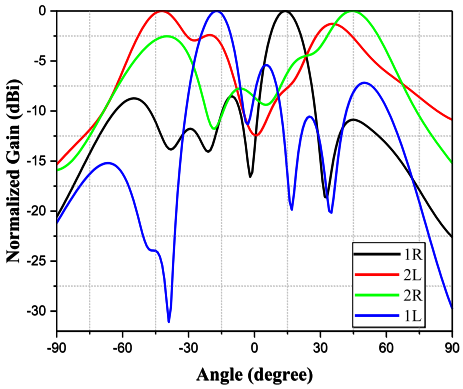

FIGURE 11. Ports switching analog beam normalization.

In Fig. 11, when the frequency is at 28 GHz, Port1 to Port4 are switched and normalized for each analog beam gain. The normalized sidelobe at Port1(1R) falls at −12.1 dBi. Next, the normalized side lobe of Port4 (1L) drops to -23 dBi. The normalized sidelobe at Port3 (2R) is -2.7 dBi. The normalized sidelobe at Port2(2L) is −1.5 dBi. The normalized sidelobe at the feed Port3(2R) is −3 dBi compared to the sidelobe. According to the simulation results presented above, it is evident that Port1 (1R) has the smallest side lobes, while Port2 (2L) and Port3 (2R) have the largest.

III. DESIGN AND EXPERIMENTAL RESULTS

A. RETURN LOSS SIMULATION AND MEASUREMENT

To evaluate the radiation pattern and the reflection coefficient measurement, the proposed 4 × 4 Butler matrix is evident that Port1 (1R) has the smallest side lobes, while Port2 (2L) and Port3 (2R) have the largest. connected to a four-element patch antenna array as in Fig. 12. The Rogers 5880 with a thickness of 0.254 mm is applied for the patch array design. The size of each patch is 4.42 × 3.37 mm^2($0.41\lambda_0 \times 0.31\lambda_0$), and the distance between each element is 5 mm.

The connection between the ground plane below the finished product entity's topmost layer and the bottom metal ground plane in Fig.12(b) through the via holes is evident, and the primary radiation sources are the four patch antennas located above the top layer. Using a ruler to mark the finished size.

Then measure the reflection coefficient and use the end launch connector to feed in the 4 × 4 Butler matrix antenna with beam switching input from Port4 is shown in Fig. 13. The Agilent network analyzer model (N5227A) was used for the measurement of the reflection coefficient, which can support the frequency of 10MHz to 67GHz. The coaxial cable uses the model (WCA205-1.2M-65GHz), the length is 120 cm, and the maximum supported frequency is 65 GHz. And use SOL (Short, Open, Load) to correct before measurement.

In the measurement and simulation comparison of the reflection coefficients of Port1 to Port4, as shown in Fig. 14. Under the condition that the reflection coefficient is required

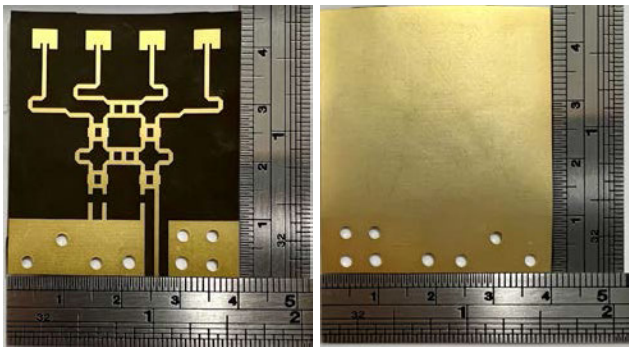

FIGURE 12. 4 × 4 Bart matrix antenna (a) Top. (b) Bottom.

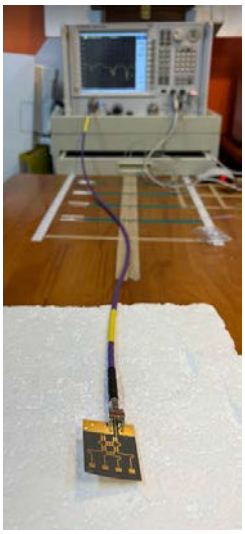

FIGURE 13. Reflection coefficient measurement.

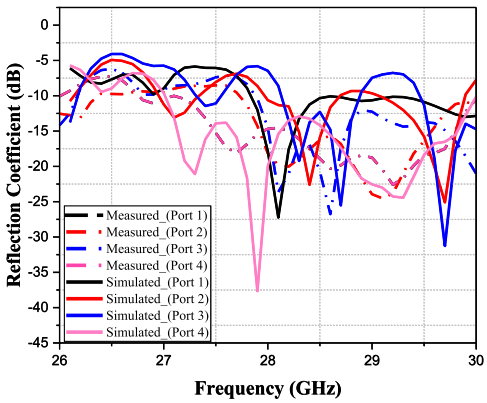

FIGURE 14. Reflection coefficient Result.

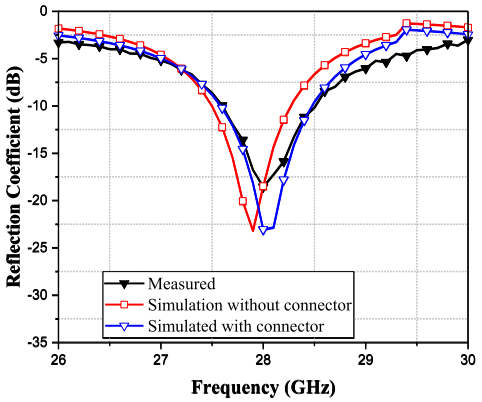

FIGURE 15. 28 GHz patch antenna reflection coefficient.

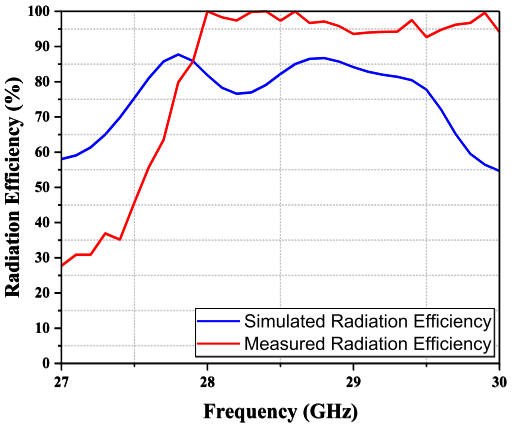

FIGURE 16. Radiation efficiency simulation and measurement

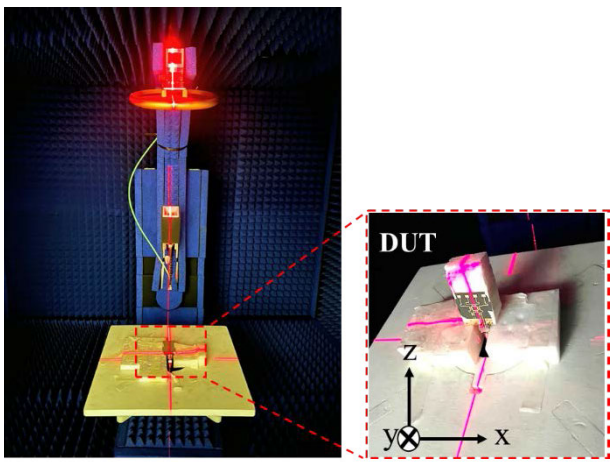

FIGURE 17. MW6 internal measurement environment.

to be less than −10dB, the measured reflection coefficient falls between 26.8-30 GHz. The reflectance coefficient simulation results for 28.5 - 29.5 GHz are within standard. However, there is a difference between the simulation and the measurement results that may be caused by the micro-curving of the substrate washed out by the antenna entity. In the comparison of the reflection coefficients of Port2, Port3, and Port4, both the measurement results and the simulation results produce multiple modes, and the measurement results produce a wider frequency band. This may be due to the measurement error of the reflection coefficient caused by the bending of the antenna structure of the substrate and the

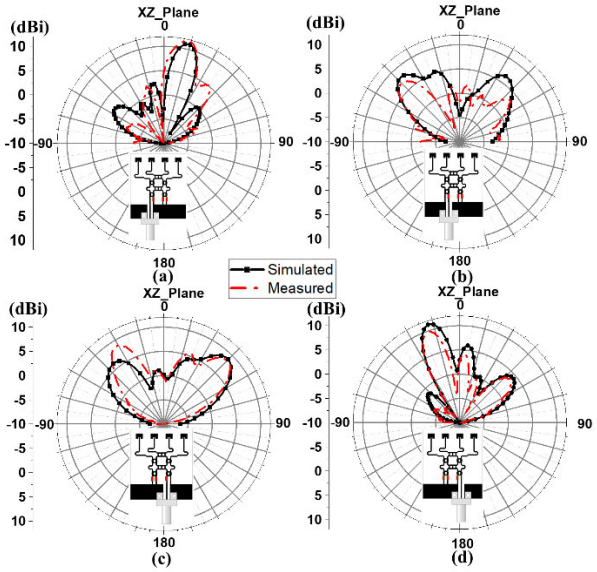

FIGURE 18. 28GH XZ plane 2D radiation. (a) Port1. (b)Port2. (c)Port3. (d)Port4.

TABLE 5. Port1 to port4 simulation and measurement beam angle integration.

	Main beam angle (Simulated)	Main beam angle (Measured)	Main beam gain (Simulated)	Main beam gain (MEASURED)
Port1	+15	+15	11 dBi	11.5dBi
Port2	-45	-46	7.9 dBi	6.9dBi
Port3	+45	+44	8.8 dBi	8.5dBi
Port4	-15	-13	11.2 dBi	9.8dBi

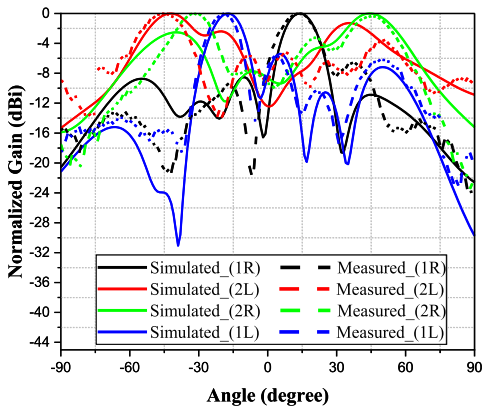

FIGURE 19. 28 GHz switching Port1 to Port4 measurement beam pattern normalization.

measurement of the effect of the end launch joint. Compared to the two modes at 28 GHz, there is a frequency offset phenomenon, and the third mode is shifted to a low frequency at 29 GHz, but these phenomena can be explained as the influence of the slight bending of the substrate washed out by the antenna entity. The 28GHz patch antenna between simulation and measurement results, as presented in Fig. 15. The observable blue line is the end launch, and the red line is without the End launch. The solid patch antenna connected to the end launch fixture is plotted in black in the graph. The reflection coefficient shows generally consistent trend results, despite a slight deviation. The final antenna radiation efficiency simulation and measurement results are shown in Figure 16. The measurement efficiency is represented by the red curve, with a frequency point of 98.2% at 28 GHz. On the other hand, the simulation efficiency is depicted by the blue curve, with a frequency point of 61.8% at 28 GHz. The difference between the simulation and measurement efficiencies is 20%, with the measurement results being higher. This discrepancy could be attributed to the material settings in the End launch not matching the actual materials, resulting in the measurement efficiency being 20% higher than the simulation efficiency.

B. BEAM DIRECTIVITY SIMULATION AND MEASUREMENT

The proposed radiation field measurements were conducted using the millimeter wave anechoic chamber MW6, covering a frequency range of 24-42 GHz. Fig. 17 comprises two photos. The left image illustrates the configuration of the cross axis at the center point where the object under test is positioned, while the right image displays the measurement setup of the MW6 millimeter- wave anechoic chamber, together with the associated X, Y, and Z axes.

In this experiment, the 2D radiation pattern of the 4 × 4 Butler matrix antenna with beam switching is used to simulate measurement and analysis. In Fig. 18, four ports in the socket are switched to generate beams, and the difference in beam angle between the 28GHz simulation and measurement is observed. Fig. 18(a) shows that the simulated and measured main lobes for input (Port 1) are almost the same. The angle of the main lobe is 15 degrees, with a simulated gain in the peak of the main lobe of 11 dBi and a measured gain in the peak of the main lobe of 11.6 dBi. In Fig. 18(b), the simulated and measured main lobes for the input port (Port 2) are very close, but there is a 1 dBi drop in gain, which may be caused by the installation error of the end launch connector. In Fig. 18(c), the simulated and measured main lobes for the input port (Port 3) are almost the same. The angle of the main lobe is 45 degrees, with a simulated peak gain of the main lobe of 8.8 dBi and a measured peak gain of the main lobe of 8.5 dBi. For the last input port (Port 4), the simulated and measured angles of the main lobe are similar, but there is a difference of 1.4 dBi in the antenna gain. This difference could be attributed to the installation error of the end launch, as shown in Fig. 18(d).

Table 5 comparison of the main beam angles measured and the simulated ideal angle of the Butler matrix antenna Port1-Port4. At 28 GHz, the beam pointing angles are +15, −46, +44, and −13. It was observed that the measured radiation pattern at Port1 showed a gain in the main lobe consistent with the simulated value. There is consistency between the simulated and measured gain of the main beam at Port1. However, in Port2, Port3, and Port4, the measured main beam angles differ by −1, +1, and -2 degrees, respectively, from the

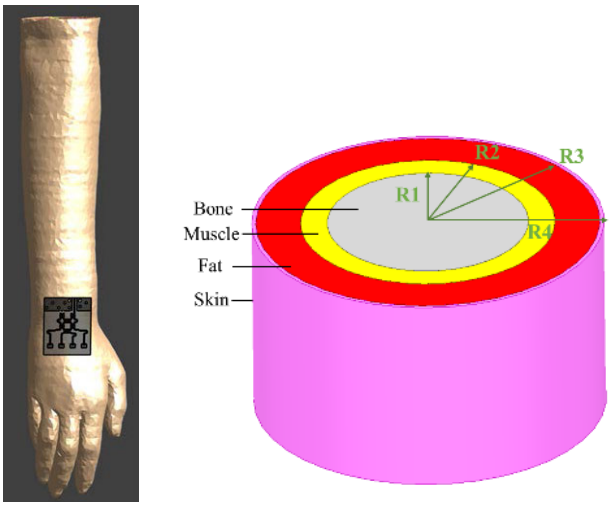

FIGURE 20. Sim4Life simulation environment. (a) Simulation of hand PD. (b) Structure of hand tissue.

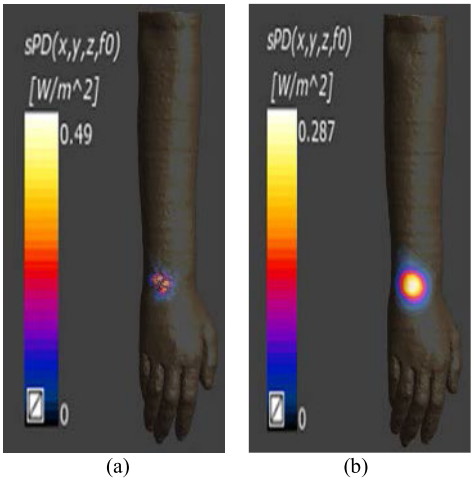

FIGURE 21. 28GHz power density simulation. (a) 1 cm^2. (b) 4 cm^2.

TABLE 6. Power density limits above 6 GHz.

	f_G (GHz)	Average Area (cm^2)	Slim(W/m^2)
ICNRP 2020 [40]	6-300 30-300	4 1	$55fG^{-0.177}$
IEEE C95.1™2019[36]	6-300 30-300	4 1	$55fG-0.177$
FCC [37]	6-300	4	10
FCC [37]	30-300	1	40

simulated ideal main beam angles. Port4 shows a difference of up to 1.4dBi, while Port1 has a measured peak gain of 11.5dBi.

As shown in Fig. 19, when the measurement frequency is at 28 GHz, the measurement beam gain is switched and

TABLE 7. Human tissue parameters.

Tissue	ε_r	σ (S/m)	Density (kg/m^3)
Skin	37.26	1.85	1109
Fat	10.59	0.37	911
Muscle	51.81	2.30	1090.4
Bone	17.73	1.08	1178.3

normalized for each of Port1 to Port4. It is observed that Port1 (1R) has the smallest partials, and Port2 (2L) and Port3 (2R) have the largest partials. The improvement in the side-flap can is achieved by increasing the beam gain of the patch antenna to increase the difference between the main beam and the side flap.

IV. SAR ANALYSIS

Due to the frequency limitation of the simulation parameters of human tissue fluids, the accuracy of the specific absorption rate (SAR) of communication products that support frequency bands above 6 GHz is questionable. However, the Federal Communications Commission (FCC) still defines the standard value as the radiated energy for wireless products operating at 1.5 to 100 GHz and conducts checks. When the transmitting power of a wireless product is larger than 20 mW and it is operated or used on a human body, the standard value that can be used is called power density (PD). The PD limit according to the FCC standard is 10 W/m^2, which is obtained from the average E = electric field, H = magnetic field, electromagnetic energy of the $4cm^2$ area above the antenna radiation hotspot of the object under test. Re is the real part, A = average area, d = distance between the antenna and the tissue, which can be calculated using (5).

FCC, IEEE, and ICNIRP 2020 are currently used, and the recently proposed limits are consolidated in Table 6. The antenna in this section is a miniaturized structure and

$$S_{inc}(A, d, \beta_X) = \frac{1}{A}\int_A \mathrm{Re}\left[\mathrm{E}(\mathrm{d}, \beta_X) \times \mathrm{H}^*(\mathrm{d}, \beta_X)\right] \cdot \hat{n} ds \tag{5}$$

can be fabricated into wrist wearable devices in the future. Therefore, the simulation software Sim4Life is used to draw the model of the hand and simulate the power density of the hand to explore the influence of electromagnetic density and the human body. Fig. 20(a) is a schematic diagram of the antenna and arm. Fig. 20(b) shows the tissue hierarchy of the Sim4Life arm model of the simulation software.

From the inside to the outside, they are bone, muscle, fat, and skin. The tissue radii of each layer are R1 to R4. Values are 12 mm, 35 mm, 42 mm and 45 mm. The parameters are shown in Table 7.

Next, simulate the power density, set the input power to 100mW, and set the distance between the antenna and the surface of the hand to 0 mm, and finally simulate the hand power density at a working frequency of 28 GHz. Fig. 21 shows the results of the simulated frequency at 28 GHz. The

TABLE 8. Comparison of literature.

Ref.	Antenna size ($\lambda_0 \times \lambda_0$)	Frequency (GHz)	Beam peak gain (dBi)	Beam angle range
[20]	3.38×3.38	26-26.4	9.9	90°
[22]	8.4 ×5.04	26.9-33.3	11.35	72°
[23]	0.47 ×1.12	79	3	93°
[24]	4.67×4.85	28-33	11.7	84°
[25]	-	27.5-28.3	-	-
[26]	5.27 ×1.96	28-32	11.2	138°
Proposed antenna	3.65×4.26	27.9-29.3	11.5	89°

power of the density is consistent with the PD specification of the FCC, measuring 0.49 W/m^2 and 0.287 W/m^2 in the areas of 1 cm^2 and 4 cm^2, respectively.

V. LITERATURE DISCUSSION

The beam-switchable 4 × 4 Butler matrix antenna is compared with international papers [20], [21], [22], [23], [24], [25], [26] published in the past three years and is summarized in Table 8. Compared to other literature on operating frequencies, the antenna size in this paper has better performance compared to the literature [22], [24], and has better peak antenna gain and beam angle range. Compared to the literature [20], [21], [23], [26], the antenna size has advantages compared to the proposed antenna size, but the antenna in this paper has a better peak gain and beam angle range. The operating frequency is 27.9-29.3 GHz for reflection coefficients below the −10 dB standard, which has a wider band compared to the literature [20], [26]. Finally, compared with other literatures, the antenna beam peak gain in this paper is 11.5dBi, and it also has higher gain performance compared with literatures [20], [21], [22].Finally, in the comparison of the beam angle, the maximum range of the antenna can reach 89 degrees, which has a wider beam angle range compared to the literature [22], [23], [24], [26]. The proposed antenna has the following characteristics. The high beam peak gain and wide beam angle range make it very competitive.

VI. CONCLUSION

Design a 28 GHz switchable 4 × 4 Butler matrix antenna using a 90-degree coupler, a 45-degree phase shifter, a crossover, and a patch antenna. This circuit can be used to switch the input port 1 to 4 to change the phase and achieve the desired beam switching ability. When the control of the analog beam steering is input to Port1, the beam can be steered at +15 degrees, and input Port2 steers the main beam to −46 degrees, while Port3 changes the angle of the main beam to +44 degrees, and finally Port4 changes it to −13 degrees. To verify the simulation results, four ports were actually switched and the radiation beam was measured. The peak beam gain was measured for each of the four input ports, 11.5 dBi for Port1, 6.9 dBi for Port2, 8.5 dBi for Port3, and 9.8 dBi for Port4. After normalizing the results of the beam gain measurement, it was observed that the side lobes of Port2 and Port3 were larger than those of Port1 and Port4. Taking into account the application of the beam switchable 4 × 4 Butler matrix antenna switchable on a wrist wearable device, this paper used Sim4Life to simulate PD of the human body. The simulated PD results at a frequency of 28 GHz were 0.49 W/m^2 for an average area of 1 cm^2 and 0.287 W/m^2 for an average area of 4 cm^2, which are consistent with the FCC power density specification standards. The 4×4 Butler matrix antenna with four-beam switching has a large bandwidth, high beam peak gain characteristics, and a switching beam angle range of 89 degrees. The use of a double-layer board on the antenna substrate makes it more cost effective than the multilayer board structure and provides a competitive advantage when applied to n258 and n261 millimeter-wave communication products.

REFERENCES

[1] J. Sui, Y. Dou, X. Mei, and K.-L. Wu, "Self-curing decoupling technique for MIMO antenna arrays in mobile terminals," *IEEE Trans. Antennas Propag.*, vol. 68, no. 2, pp. 838–849, Feb. 2020.

[2] W. Wang, Y. Wu, W. Wang, and Y. Yang, "Isolation enhancement in dual-band monopole antenna for 5G applications," *IEEE Trans. Circuits Syst. II, Exp. Briefs*, vol. 68, no. 6, pp. 1867–1871, Jun. 2021.

[3] A. Khan, S. Bashir, S. Ghafoor, and K. K. Qureshi, "Mutual coupling reduction using ground stub and EBG in a compact wideband MIMO-antenna," *IEEE Access*, vol. 9, pp. 40972–40979, 2021.

[4] Y. He, J. Huang, W. Li, L. Zhang, S.-W. Wong, and Z. N. Chen, "Hybrid method of artificial neural network and simulated annealing algorithm for optimizing wideband patch antennas," *IEEE Trans. Antennas Propag.*, vol. 72, no. 1, pp. 944–949, Jan. 2024.

[5] S. Feng, L. Zhang, Z. Weng, and Y.-C. Jiao, "A wideband differential-fed microstrip patch antenna based on quad-mode resonance with radiation patterns correction," *IEEE Trans. Antennas Propag.*, vol. 71, no. 6, pp. 5404–5409, Jun. 2023.

[6] K. Ma, N. Yan, and Y. Wang, "Recent progress in SISL circuits and systems: Review of passive and active circuits demonstrating SISL's low loss and self-packaging and showcasing the merits of metallic, shielded, suspended lines," *IEEE Microw. Mag.*, vol. 22, no. 4, pp. 49–71, Apr. 2021.

[7] G. Yang, Y. Zhang, and S. Zhang, "Wide-band and wide-angle scanning phased array antenna for mobile communication system," *IEEE Open J. Antennas Propag.*, vol. 2, pp. 203–212, 2021.

[8] Y. Su and C. Chang, "Designs of deformed eight-way Butler matrix with port reduction for massive array beamforming," *IET Microw., Antennas Propag.*, vol. 13, no. 6, pp. 864–869, May 2019.

[9] S. Karamzadeh, V. Rafii, M. Kartal, and B. S. Virdee, "Modified circularly polarised beam steering array antenna by utilised broadband coupler and 4 × 4 Butler matrix," *IET Microw., Antennas Propag.*, vol. 9, no. 9, pp. 975–981, Jun. 2015.

[10] C. Chang, C. Lin, and W. Cheng, "Fully integrated 60 GHz switched-beam phased antenna array in glass-IPD technology," *Electron. Lett.*, vol. 51, no. 11, pp. 804–806, May 2015.

[11] K. Liu, S. Yang, S.-W. Qu, C. Chen, and Y. Chen, "Phased hemispherical lens antenna for 1-D wide-angle beam scanning," *IEEE Trans. Antennas Propag.*, vol. 67, no. 12, pp. 7617–7621, Dec. 2019.

[12] L. Yin, P. Yang, Y. Gan, F. Yang, S. Yang, and Z. Nie, "A low cost, low in-band RCS microstrip phased-array antenna with integrated 2-bit phase shifter," *IEEE Trans. Antennas Propag.*, vol. 69, no. 8, pp. 4517–4526, Aug. 2021.

[13] H.-J. Dong, Y.-B. Kim, and H. L. Lee, "Reconfigurable quad-polarization switched beamforming antenna with crossed inverted-V array and dual-butler matrix," *IEEE Trans. Antennas Propag.*, vol. 70, no. 4, pp. 2708–2716, Apr. 2022.

[14] S. Li, Z. Liu, S. Fu, Y. Wang, and F. Xu, "Intelligent beamforming via physics-inspired neural networks on programmable metasurface," *IEEE Trans. Antennas Propag.*, vol. 70, no. 6, pp. 4589–4599, Jun. 2022.
[15] Z. Tang and Y. Dong, "A Ka-band antenna array based on wide-beamwidth magnetoelectric dipole," *IEEE Antennas Wireless Propag. Lett.*, vol. 21, pp. 501–505, 2022.
[16] Y. Yang, Y. F. Pan, S. Y. Zheng, W. Hong, and W. S. Chan, "Analytical design method and implementation of broadband 4×4 nolen matrix," *IEEE Trans. Microw. Theory Techn.*, vol. 70, no. 1, pp. 343–355, Jan. 2022.
[17] H. Zhu, T. Zhang, and Y. J. Guo, "Wideband hybrid couplers with unequal power division/arbitrary output phases and applications to miniaturized nolen matrices," *IEEE Trans. Microw. Theory Techn.*, vol. 70, no. 6, pp. 3040–3053, Jun. 2022.
[18] P. Li, H. Ren, and B. Arigong, "A symmetric beam-phased array fed by a nolen matrix using 180° couplers," *IEEE Microw. Wireless Compon. Lett.*, vol. 30, no. 4, pp. 387–390, Apr. 2020.
[19] J. Hirokawa and N. J. G. Fonseca, "Generalized one-dimensional parallel switching matrices with an arbitrary number of beams," *IEEE J. Microw.*, vol. 1, no. 4, pp. 975–988, Oct. 2021.
[20] S. Kim, S. Yoon, Y. Lee, and H. Shin, "A miniaturized Butler matrix based switched beamforming antenna system in a two-layer hybrid stackup substrate for 5G applications," *Electronics*, vol. 8, no. 11, p. 1232, Oct. 2019.
[21] A. Tamayo-Domínguez, J.-M. Fernández-González, and M. Sierra-Castañer, "Monopulse radial line slot array antenna fed by a 3-D-printed cavity-ended modified Butler matrix based on gap waveguide at 94 GHz," *IEEE Trans. Antennas Propag.*, vol. 69, no. 8, pp. 4558–4568, Aug. 2021.
[22] I. Afifi and A.-R. Sebak, "Wideband 4×4 Butler matrix in the printed ridge gap waveguide technology for millimeter-wave applications," *IEEE Trans. Antennas Propag.*, vol. 68, no. 11, pp. 7670–7675, Nov. 2020.
[23] N. T. Tuan, K. Sakakibara, K. Iwasa, T. Okunaga, N. Kikuma, and Y. Sugimoto, "Millimeter-wave Butler matrix beamforming circuit using finline in double-layer dielectric substrate," *IEEE Open J. Antennas Propag.*, vol. 1, pp. 579–589, 2020.
[24] N. Ashraf, A.-R. Sebak, and A. A. Kishk, "PMC packaged single-substrate 4×4 Butler matrix and double-ridge gap waveguide horn antenna array for multibeam applications," *IEEE Trans. Microw. Theory Techn.*, vol. 69, no. 1, pp. 248–261, Jan. 2021.
[25] F. Pizarro, D. Ramírez-Gil, A. Algaba-Brazález, L. F. Herrán-Ontanón, and E. Rajo-Iglesias, "Comparison study of 4×4 Butler matrices in microstrip technologies for Ka-band," *AEU Int. J. Electron. Commun.*, vol. 122, Jul. 2020, Art. no. 153248.
[26] M. M. Pezhman, A.-A. Heidari, and A. Ghafoorzadeh-Yazdi, "A compact 4×4 SIW beamforming network for 5G applications," *AEU Int. J. Electron. Commun.*, vol. 135, Jun. 2021, Art. no. 153714.
[27] W. Rotman and R. Turner, "Wide-angle microwave lens for line source applications," *IEEE Trans. Antennas Propag.*, vol. AP-11, no. 6, pp. 623–632, Nov. 1963.
[28] Y. Yu, H. Luyen, and N. Behdad, "A wideband millimeter-wave Rotman lens multibeam array using substrate integrated coaxial line (SICL) technology," *IEEE Trans. Antennas Propag.*, vol. 69, no. 11, pp. 7532–7542, Nov. 2021.
[29] J. Li, C. He, H. Fan, and R. Jin, "Gain-equalized multibeam antenna fed by a compact dual-layer Rotman lens at Ka -band," *IEEE Trans. Antennas Propag.*, vol. 70, no. 3, pp. 2307–2311, Mar. 2022.
[30] S. K. Karki, M. Varonen, M. Kaunisto, A. Rantala, M. Lahti, A. Lamminen, J. Holmberg, M. Kantanen, J. Ala-Laurinaho, and V. Viikari, "Beam-reconfigurable antenna based on vector modulator and Rotman lens on LTCC," *IEEE Access*, vol. 9, pp. 52872–52882, 2021.
[31] H.-T. Chou and D. Torrungrueng, "Development of 2-D generalized trifocal Rotman lens beamforming network to excite conformal phased arrays of antennas for general near/far-field multi-beam radiations," *IEEE Access*, vol. 9, pp. 49176–49188, 2021.
[32] N.-C. Liu, C.-C. Tien, C.-Y. Chang, H.-W. Ling, C.-W. Chiu, and J.-H. Tarng, "Millimeter-wave 2-D beam-switchable and scalable phased antenna array," *IEEE Trans. Antennas Propag.*, vol. 69, no. 12, pp. 8997–9002, Dec. 2021.
[33] H. Liu, H. Zhang, S.-J. Fang, and Z. Wang, "Compact broadband 3×3 nolen matrix with flat output ports phase differences," *Prog. Electromagn. Res. Lett.*, vol. 103, pp. 49–56, 2022.
[34] A. K. Vallappil, M. K. A. Rahim, B. A. Khawaja, N. A. Murad, and M. G. Mustapha, "Butler matrix based beamforming networks for phased array antenna systems: A comprehensive review and future directions for 5G applications," *IEEE Access*, vol. 9, pp. 3970–3987, 2021.
[35] C. A. Balanis, *Antenna Theory: Analysis and Design*. Hoboken, NJ, USA: Wiley, 2015.
[36] W. H. Bailey, "Synopsis of IEEE STD C95. 1-2019 IEEE standard for safety levels with respect to human exposure to electric, magnetic, and electromagnetic fields, 0 Hz to 300 GHz," *IEEE Access*, vol. 7, pp. 171346–171356, 2019.
[37] B. Xu, K. Zhao, Z. Ying, D. Sjöberg, W. He, and S. He, "Analysis of impacts of expected RF EMF exposure restrictions on peak EIRP of 5G user equipment at 28 GHz and 39 GHz bands," *IEEE Access*, vol. 7, pp. 20996–21005, 2019.
[38] N. Bayat-Makou and A. A. Kishk, "Realistic air-filled TEM printed parallel-plate waveguide based on ridge gap waveguide," *IEEE Trans. Microw. Theory Techn.*, vol. 66, no. 5, pp. 2128–2140, 2018.
[39] M. M. M. Ali and A. Sebak, "Compact printed ridge gap waveguide crossover for future 5G wireless communication system," *IEEE Microw. Wireless Compon. Lett.*, vol. 28, no. 7, pp. 549–551, 2018.

MING-AN CHUNG (Senior Member, IEEE) received the B.Eng. and M.Eng. degrees in electronic engineering from Chang Gung University, Taoyuan, Taiwan, in 2003 and 2005, respectively, and the D.Eng. degree in electrical engineering from the National Taiwan University of Science and Technology (NTUST), Taipei, Taiwan, in 2016. He is currently an Associate Professor with the Department of Electronic Engineering, National Taipei University of Technology (NTUT), where he is also the Leader of the Innovation Wireless Communication and Electromagnetic Applications Laboratory. His research interests include wireless communication propagation, intelligent robotics, self-driving vehicles, antenna design for various mobile and wireless communications, electromagnetic theory, and applications. He is a Reviewer of many scientific journals, including IEEE TRANSACTIONS ON ANTENNAS AND PROPAGATION, IEEE TRANSACTIONS ON INDUSTRIAL INFORMATICS, *Journal of Intelligent and Robotic Systems*, *IET Microwaves, Antennas & Propagation*, IEEE ANTENNAS AND WIRELESS PROPAGATION LETTERS, *International Review of Electrical Engineering*, *International Journal on Communications Antenna and Propagation*, and *AEÜ-International Journal of Electronics and Communications*, and many international conferences, including ICRA, ICCE-TW, RFIT, ICBEB, EMCAR, and SNSP.

CHIA-WEI LIN received the B.S. and M.S. degrees from Chung Yuan Christian University, in 2007. He is currently pursuing the Ph.D. degree in electrical engineering with the National Taipei University of Technology. His research interests include wireless communication propagation research, antenna design, intelligent robotics research, self-driving vehicle research, embedded systems, and deep learning.

CHIH-WEI YANG received the B.S. degree from St. John's University of Technology, in 2016. He is currently pursuing the M.S. degree in electronic engineering with the National Taipei University of Technology. His research interests include high-frequency device research, near-field communication research, and RFIC design research.